Full-system RANS of the HyShot II scramjet Part 2: Reactive cases

By V. E. Terrapon, R. Pečnik, F. Ham AND H. Pitsch

1. Motivation and objective

This is the second of a two-part study of the HyShot II scramjet. While the first part focused on non-reacting cases, combustion and heat release are considered here. The HyShot II model scramjet has been the subject of many studies. Experimentally, both flight (e.g., Hass *et al.* 2005; Smart *et al.* 2006) and ground (e.g., Gardner *et al.* 2004; Schramm *et al.* 2008) measurements have provided useful data on the operation of high-speed air-breathing vehicles. However, many critical aspects of the combustion processes are not directly accessible to experimental measurements. Relying on computation is therefore a useful complement for physical understanding, design and failure analysis. This explains the large number of computational studies on the HyShot II system, ranging from quasi-one-dimensional models (Birzer & Doolan 2007) to, more recently, LES simulations (Fureby *et al.* 2010; Ingenito *et al.* 2010).

The critical aspect in scramjet propulsion is that combustion takes place at supersonic speeds. Therefore, the flow has a very short residence time, i.e., of the order of 1ms, during which air and fuel must mix on a molecular level, and chemical reactions have to be completed before leaving the engine. Moreover, supersonic flows are usually accompanied by shocks that interact with both the turbulence and the flame. The kinetic energy of the free stream of air entering the propulsion engine is of the same order of magnitude as the combustion heat release. This results in a small net thrust compared to the aerodynamic drag, and minimizing this drag becomes critical. On the other hand, an excessive heat release can lead to the unstart phenomenon, i.e., the choking of the engine, that causes a sudden drop in thrust and large mechanical loads on the structure. Performance optimization thus requires maximizing thrust without crossing the unstart bound. Since heat release is at the heart of a scramjet operation and the main contributor to unstart, the implementation of an accurate combustion model for supersonic combustion is critical.

A comparison between flight data and CFD calculations was performed by Boyce *et al.* (2003), but showed a consistently lower pressure level than the experimental measurements. Steelant *et al.* (2006) and Karl *et al.* (2006) performed RANS simulations of the HyShot II configuration and compared these with both flight and ground experiments. This work was then extended in Karl *et al.* (2008), where a systematic study of inflow conditions and turbulence models was performed. The combustion model used in these studies relied on finite-rate chemistry and the explicit transport of the involved species. The turbulence-chemistry interaction was modeled using a multivariate assumed probability distribution function (PDF) introduced by Baurle & Girimaji (2003). A similar approach, but with a different code, was used by Kindler *et al.* (2008), who demonstrated that the use of a closure model for the species source term and an accurate mechanism are critical to accurately reproduce the physics. Nevertheless, some authors found good agreement with experiments while neglecting appropriate closure. Kodera *et al.* (2005), for instance, investigated different injection strategies in a modified version of the HyShot

combustor. Other approaches to deal with this closure problem have been followed for supersonic combustion, like the Eddy Dissipation Concept model (Chakraborty *et al.* 2000), or with closure based on transported PDF (Baurle *et al.* 1995). Some authors have also used the Linear Eddy Mixing model (LEM) (Genin *et al.* 2004). But due to the strong non-linearity of the source term and the wide range of time scales associated with the chemistry, those equations are very stiff and difficult to solve. Moreover, due to very short residence times in such high-speed flows, flame stabilization mechanisms are governed by auto-ignition. It is critical to model accurately such ignition and extinction phenomena in order to predict the stability of scramjet combustion. Therefore, prediction of flame stabilization requires a detailed description of the chemical kinetics. While a model transporting all involved species can easily be extended to more detailed chemical mechanisms, it quickly becomes computationally intractable, especially when complex fuels are considered. Since combustion in a scramjet is mostly mixing controlled, it is also critical to accurately predict turbulent mixing. Very recently some authors have relied on large eddy simulation (LES) and showed that capturing turbulent eddies improves mixing and, thus, combustion predictions (Ingenito *et al.* 2010; Fureby *et al.* 2010).

All the aforementioned studies have relied on transporting all involved species and some closure models for the turbulence-chemistry interaction. An alternative approach is based on the flamelet concept (Peters 2000; Pitsch 2006), which assumes that the chemical time scales are shorter than the turbulent time scales of the energy-containing eddies so that the flame can be approximated as one-dimensional. The flamelet approach allows the computation of the chemistry to be performed independently of the combustor simulation and stored in tabulated form as a function of a limited number of scalars. During the actual scramjet simulation, the quantities of interest are read and interpolated, thus dramatically decreasing the computational cost and allowing the use of complex chemical mechanisms. However, typical implementations of the flamelet model are based on a low Mach number assumption, explaining the still very limited number of studies of high-speed flows using this approach (Berglund & Fureby 2007; Terrapon *et al.* 2009).

A similar combustion model based on tabulated chemistry, as described in the next section, is presented here. The model is then used to simulate the heat release in the HyShot II combustor. First, a constant equivalence ratio $\phi = 0.3$ is used and results are compared with the experimental measurements performed in the High Enthalpy Shock Tunnel (HEG) of the German Aerospace Center (DLR) (Gardner *et al.* 2004). In a second step, the fuel flow rate is increased and the evolution of the flow topology towards unstart is investigated.

2. Combustion Model

2.1. *Equations*

The conserved Favre-averaged variables $Q = \{\bar{\rho}, \bar{\rho}\widetilde{u}_i, \bar{\rho}\widetilde{E}, \bar{\rho}\widetilde{Z}, \bar{\rho}\widetilde{Z''^2}, \bar{\rho}\widetilde{C}\}^T$ are solved in conservative form, where $\bar{\rho}$ is the density, $\widetilde{u}_i$ the components of the velocity vector, $\widetilde{E}$ the total energy, including the chemical energy, $\widetilde{Z}$ the mixture fraction, $\widetilde{Z''^2}$ the variance of the mixture fraction and $\widetilde{C}$ a progress variable. The transport equations are

$$\frac{\partial \bar{\rho}}{\partial t} + \frac{\partial \bar{\rho}\widetilde{u}_j}{\partial x_j} = 0, \tag{2.1}$$

$$\frac{\partial \bar{\rho}\widetilde{u}_i}{\partial t} + \frac{\partial \bar{\rho}\widetilde{u}_i\widetilde{u}_j}{\partial x_j} + \frac{\partial \bar{p}}{\partial x_i} = \frac{\partial}{\partial x_j}\left[(\widetilde{\mu}+\mu_t)\left(\frac{\partial \widetilde{u}_i}{\partial x_j} + \frac{\partial \widetilde{u}_j}{\partial x_i} - \frac{2}{3}\delta_{ij}\frac{\partial \widetilde{u}_k}{\partial x_k}\right) - \frac{2}{3}\bar{\rho}k\delta_{ij}\right], \quad (2.2)$$

$$\begin{aligned}\frac{\partial \bar{\rho}\widetilde{E}}{\partial t} + \frac{\partial \bar{\rho}\widetilde{u}_j\widetilde{E}}{\partial x_j} =& \frac{\partial}{\partial x_j}\left[\left(\widetilde{\frac{\lambda}{c_p}} + \frac{\mu_t}{Pr_t}\right)\frac{\partial \widetilde{h}}{\partial x_j}\right] + \frac{\partial}{\partial x_j}\left[\sum_{k=1}^{N}\left(\bar{\rho}\widetilde{D}_k - \widetilde{\frac{\lambda}{c_{p_k}}}\right)\widetilde{h}_k\frac{\partial \widetilde{Y}_k}{\partial x_j}\right] \\ &+ \frac{\partial}{\partial x_j}\left[\left(\widetilde{\mu} + \frac{\mu_t}{\sigma_k}\right)\frac{\partial k}{\partial x_j} - \widetilde{u}_j\bar{p} + \widetilde{u}_i\left(\bar{\tau}_{ij} + \bar{\tau}_{ij}^R\right)\right],\end{aligned} \quad (2.3)$$

$$\frac{\partial \bar{\rho}\widetilde{Z}}{\partial t} + \frac{\partial \bar{\rho}\widetilde{u}_j\widetilde{Z}}{\partial x_j} = \frac{\partial}{\partial x_j}\left[\left(\bar{\rho}\widetilde{D} + \frac{\mu_t}{Sc_t}\right)\frac{\partial \widetilde{Z}}{\partial x_j}\right], \quad (2.4)$$

$$\frac{\partial \bar{\rho}\widetilde{Z''^2}}{\partial t} + \frac{\partial \bar{\rho}\widetilde{u}_j\widetilde{Z''^2}}{\partial x_j} = \frac{\partial}{\partial x_j}\left[\left(\bar{\rho}\widetilde{D} + \frac{\mu_t}{Sc_t}\right)\frac{\partial \widetilde{Z''^2}}{\partial x_j}\right] + 2\frac{\mu_t}{Sc_{t_2}}\frac{\partial \widetilde{Z}}{\partial x_j}\frac{\partial \widetilde{Z}}{\partial x_j} - \bar{\rho}\widetilde{\chi}, \quad (2.5)$$

$$\frac{\partial \bar{\rho}\widetilde{C}}{\partial t} + \frac{\partial \bar{\rho}\widetilde{u}_j\widetilde{C}}{\partial x_j} = \frac{\partial}{\partial x_j}\left[\left(\bar{\rho}\widetilde{D} + \frac{\mu_t}{Sc_t}\right)\frac{\partial \widetilde{C}}{\partial x_j}\right] + \bar{\dot{\omega}}_C, \quad (2.6)$$

where μ and μ_t are the laminar and turbulent viscosity, k the turbulent kinetic energy, λ the thermal diffusivity, c_p the specific heat capacity at constant pressure, Pr_t a turbulent Prandtl number, h the sensible and chemical enthalpy, Y_k the species mass fractions, σ_k the turbulent kinetic energy Schmidt number, τ_{ij} and τ_{ij}^R the viscous and Reynolds stresses as defined on the right-hand side of Eq. (2.2), D the diffusion coefficient for the scalars, Sc_t a turbulent Schmidt number, χ the scalar dissipation rate and $\dot{\omega_C}$ the source term for the progress variable. The laminar properties μ, λ, c_p are computed using mixing rules (Bird *et al.* 2007), thus accounting for changes in composition and temperature. The turbulent viscosity μ_t and the kinetic energy k are computed with an adequate turbulence model.

Notice that the summation on the right-hand side of Eq. (2.3) vanishes under the unity Lewis number assumption $Le_k = 1$, so that the species mass fractions do not need to be explicitly computed. Although the unity Lewis number assumption is not valid in the case of hydrogen, it is assumed that turbulent diffusion is much higher than the laminar diffusion, so this term can be neglected.

In order to close this system, the pressure and the temperature need to be determined. This is achieved, as explained below, by using an equation of state and the definition of the energy and enthalpy.

2.2. *Flamelet-based combustion model*

The combustion model used here is based on a Flamelet/Progress Variable approach (Pierce & Moin 2004; Ihme *et al.* 2005), in which the chemistry is pre-computed and tabulated as a series of laminar flamelet solutions for a given set of boundary conditions and background pressure. In the low Mach number flamelet implementation, the temperature and the species mass fraction are assumed to depend only on a transported scalar, traditionally the mixture fraction, and its dissipation rate. Chemical tables are then constructed assuming constant background pressure. However, the low Mach number assumptions no longer hold at supersonic speed where compressibility effects and

viscous heating play an important role. Therefore, the temperature is here computed from the transported total energy $\widetilde{E}$ and the species mass fractions $\widetilde{Y}_k$. Further, the model is extended for the auto-ignition regime with arguments similar to those in the model developed by Cook *et al.* (2007) for ignition in HCCI engines. Assumed PDFs are introduced to account for the turbulence/chemistry interaction. Typically, a β-PDF is assumed for the mixture fraction Z and a δ-PDF for the progress variable C. Therefore, the flamelet library is parametrized by the mean mixture fraction $\widetilde{Z}$, the variance of the mixture fraction $\widetilde{Z''^2}$, and the mean progress variable $\widetilde{C}$.

The total energy $\widetilde{E}$ of the N species mixture is defined as the sum of the internal energy including chemical energy $\widetilde{e}$, the kinetic energy $1/2\widetilde{u}_j^2$ and the turbulent kinetic energy k. The internal energy is

$$\widetilde{e} = \widetilde{h} - \widetilde{RT} = \sum_{k=1}^{N} \widetilde{Y_k h_k} - \widetilde{RT}, \tag{2.7}$$

where $R = R_u \sum_k Y_k/W_k$ is the gas constant, R_u the universal gas constant, W_k the molecular weight of species k and T the temperature. The specific enthalpy of species k is computed as

$$h_k(T) = \Delta h_k^0(T_{ref}) + \int_{T_{ref}}^{T} c_{p,k}(T')dT', \tag{2.8}$$

using its specific heat capacity $c_{p,k}$ and heat of formation $\Delta h_k^0(T_{ref})$. Due to the wide range of temperature in a high-speed flow, the dependence of the heat capacity on temperature must be considered.

Since the total energy is a non-linear function of the temperature, an iterative method like Newton-Raphson is required to compute the temperature given $\widetilde{E}$. In order to eliminate this expensive iterative step, an alternate approach is proposed. For a given mixture, i.e., for fixed $\widetilde{Z}$, $\widetilde{Z''^2}$ and $\widetilde{C}$, Eq. (2.7) can be approximated as

$$\widetilde{e} = \widetilde{e}_0 + \int_{T_0}^{T} \widetilde{c}_v(T)dT = \widetilde{e}_0 + \int_{T_0}^{T} \frac{\widetilde{R}_0}{\widetilde{\gamma}(T) - 1} dT, \tag{2.9}$$

where $\widetilde{\gamma}$ is the ratio of the specific heats. $\widetilde{\gamma}$ can be expanded about the flamelet solution using a linear expansion in temperature,

$$\widetilde{\gamma}(T) = \widetilde{\gamma}_0 + a_\gamma (T - T_0), \tag{2.10}$$

where the subscript $_0$ denotes the value at the flamelet solution. The values of $\widetilde{e}_0$, $\widetilde{R}_0$, $\widetilde{\gamma}_0$, a_γ and T_0 can be computed during a preprocessing step and tabulated in the chemistry library. This approximation leads to an analytical relationship between temperature and specific energy

$$\widetilde{e} = \widetilde{e}_0 + \frac{\widetilde{R}}{a_\gamma} \ln\left(1 + \frac{a_\gamma (T - T_0)}{\widetilde{\gamma}_0 - 1}\right), \tag{2.11}$$

$$T = T_0 + \frac{\widetilde{\gamma}_0 - 1}{a_\gamma} \left(\mathrm{e}^{a_\gamma (\widetilde{e} - \widetilde{e}_0)/\widetilde{R}} - 1\right). \tag{2.12}$$

In order to completely close the system of equations (2.1)-(2.6), the equation of state for an ideal gas is used to compute the pressure

$$\bar{p} = \bar{\rho} \widetilde{RT}. \tag{2.13}$$

A similar expansion around the flamelet solution is used for $\widetilde{\mu}$ and $\widetilde{\lambda/c_p}$, where the functional form of the expansion is based on a power law

$$\widetilde{\mu} = \widetilde{\mu}_0 \left(\frac{T}{T_0} \right)^{a_\mu}, \tag{2.14}$$

$$\widetilde{\lambda/c_p} = \widetilde{\lambda/c_p}_0 \left(\frac{T}{T_0} \right)^{a_\lambda}. \tag{2.15}$$

In practice, the constants a_μ and a_λ are kept constant at a value of 0.7 and 0.62, respectively.

2.3. *Pressure rescaling of the progress variable source term*

It can be shown that the source term for the progress variable is very sensitive to pressure. Therefore, we introduce a rescaling of the progress variable source term to account for pressure variations due to compressibility. Because the majority of the fundamental chemical reactions controlling the oxidation of hydrogen involve bimolecular reactions, the source term scales with the square of the pressure. We can thus rescale the source term in Eq. (2.6) as follows:

$$\bar{\dot{\omega}}_C = \bar{\dot{\omega}}_{C_0} \frac{p^2}{p_0^2}, \tag{2.16}$$

where $\bar{\dot{\omega}}_{C_0}$ is the tabulated source term computed at a background pressure p_0. A similar approach is being developed to account for the dependence of the source term on temperature.

3. Results

The same configuration and conditions as in part I are investigated here. The numerical implementation and the meshes used are also identical (see also Pecnik *et al.* 2009). The k-ω SST model is used for all simulations. Note that the scalars for the combustion model, i.e., $\widetilde{Z}$, $\widetilde{Z''^2}$ and $\widetilde{C}$, are solved fully coupled with the Navier-Stokes equations. The turbulent Schmidt and Prandtl numbers are, respectively, $Sc_t = Sc_{t_2} = 0.5$ and $Pr_t = 0.5$.

The chemistry model is based on the GRI-Mech v3.0 mechanism modified with new OH thermodynamics data (Herbon *et al.* 2002) and new H+O_2+M rates (Bates *et al.* 2001). The nine species considered are nitrogen (N_2), molecular and atomic oxygen and hydrogen (O_2, O, H_2, H), water (H_2O), hydrogen peroxide (H_2O_2), and the hydroxyl and hydroperoxyl radicals (OH, HO_2). The mechanism consists of 28 reactions. Nitrogen chemistry is not considered in this model. The chemistry table has been created from a series of laminar diffusion flamelet computations using the FlameMaster code. The pressure was chosen to correspond to an approximate average combustor pressure of $P = 1.5$ bar, whereas the boundary conditions were set to $T_O = 1300$ K for the oxidizer and $T_F = 300$ K for the fuel. The progress variable is defined as the mass fraction of water, i.e., $C = Y_{H_2O}$.

3.1. *Nominal fuel flow rate*

As a first step, the model is compared to experimental data from DLR for the nominal fuel flow rate corresponding to an equivalence ratio of $\phi = 0.3$ (Hannemann *et al.* 2010). This case has been computed with two different meshes (see part I). The first one

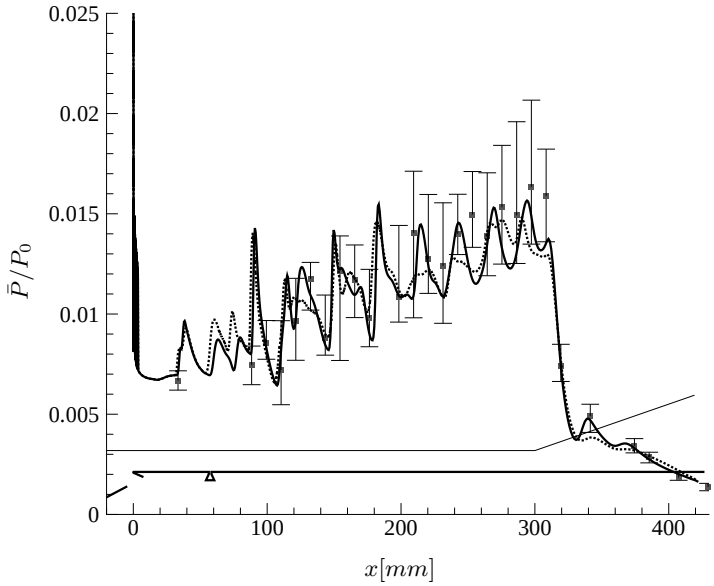

FIGURE 1. Pressure along the bottom wall of the combustor between two hydrogen injectors. The pressure is normalized by the total pressure $P_0 = 17.7$ MPa. One eighth of the combustor without side walls, continuous line; one half of the combustor with side walls, dotted line; and experimental data, symbols with error bars. The location of the injector is indicated by the geometry schematics at the bottom of the figure.

corresponds to one eighth of the combustor span including half an injector. Symmetry boundary conditions are used for the sides of the domain in the spanwise direction. In the second configuration, half of the combustor and 2 injectors are included in the computational domain. In addition, a side wall with a no-slip boundary condition is used on one side, while a symmetry condition is used for the other side. This second configuration introduces additional physics as a shock originates from the leading edge of the side wall and propagates throughout the combustion chamber.

Figure 1 shows the normalized pressure trace at the bottom wall of the combustor (body side) along the centerline (i.e., between two injectors). In this and the following figures the position of the injector and the beginning of the exhaust nozzle are indicated in the combustor schematics. The error bars on the experimental measurements result from variability across different runs (different total conditions) and from the time fluctuations over the duration of the measurements. Note that the large variability observed across runs is mostly due to variability in the fuel injection pressure. The results agree well with the experimental measurements, with a slightly lower computed pressure towards the end of the straight section of the combustor. The two computational domains (with and without side walls) lead to a similar pressure level, but small differences can be observed.

Slightly larger discrepancies are seen in the wall heat flux (Figure 2). In particular, the overall heat flux in the downstream half of the combustor is slightly overpredicted by the computation. The computed heat flux also indicates small differences between the two computational domains. These discrepancies originate from the additional shock created by the leading edge of the side walls (half combustor case), as illustrated by Figure 3. Contours of pressure are plotted in a plane parallel to the bottom wall at a wall-normal distance of $y/d = 0.25$, where $d = 2$ mm is the injector diameter. The

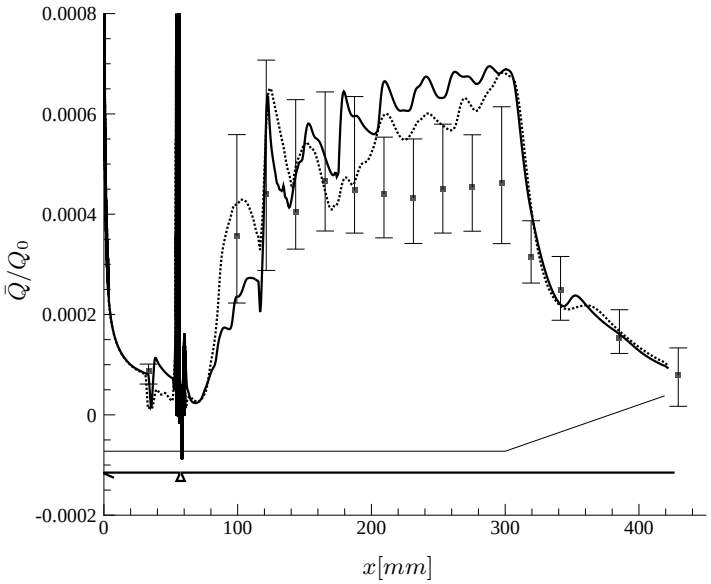

FIGURE 2. Heat flux along the bottom wall of the combustor behind one injector. The heat flux is normalized by a reference value $Q_0 = 12.37 \cdot 10^9$ W/m^2 . One eighth of the combustor without side walls, continuous line; one half of the combustor with side walls, dotted line; and experimental data, symbols with error bars.

shock train created by the leading edge of the bottom wall interacts with the bow shock created by the injected fuel and forms a complex shock system throughout the combustion chamber. Because the boundary layer is first laminar and transitions to turbulence only shortly before the injection, a small separation region forms at the foot of the first shock reflection. Due to the symmetry boundary conditions, the first configuration shows a very symmetric shock system. However, when a side wall is considered (configuration 2), this shock system is disturbed by the side shock and loses its symmetry (see Figure 3(b)). This side shock impinges on the second injector, creating a local pressure rise, which in turn increases locally the combustion rate. This is illustrated in Figure 4 by the OH mass fraction contour that shows a slightly higher OH level upstream of the second injector (Figure 4(b)).

While it is clear that accounting for the side walls is important in order to capture the details of the physics, the overall heat release is very similar for both configurations, as indicated by the similar pressure level. Therefore, the following analysis on the fuel flow increase is performed in the first configuration, i.e., one eighth of the combustor without side walls.

3.2. *Fuel flow rate increase*

In order to investigate the inception of the unstart phenomenon by thermal choking, the fuel flow rate is incrementally increased from $\phi = 0.3$ to $\phi = 0.5$. The corresponding total pressures in the plenum of the injector are summarized in Table 3.2, while the total temperature is set to $T_{0,inj} = 300$ K for all cases. Figure 5 shows the pressure along the center line at the bottom wall of the combustor for different equivalence ratios. From $\phi = 0.3$ to $\phi = 0.4$, the pressure level simply rises but shows a qualitative similar profile. However, an additional increase of the fuel flow rate leads to a very different pressure profile. The maximum pressure rises dramatically and a normal shock forms.

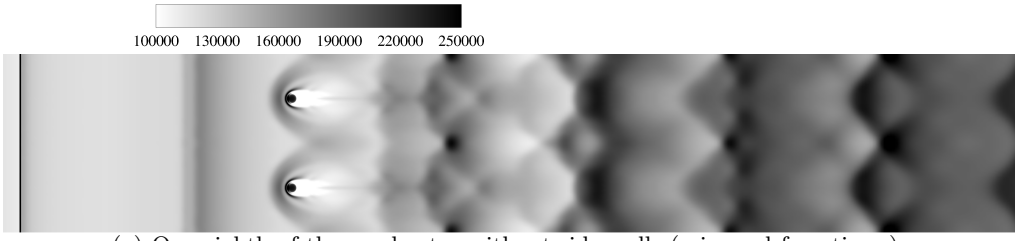

(a) One eighth of the combustor without side walls (mirrored four times).

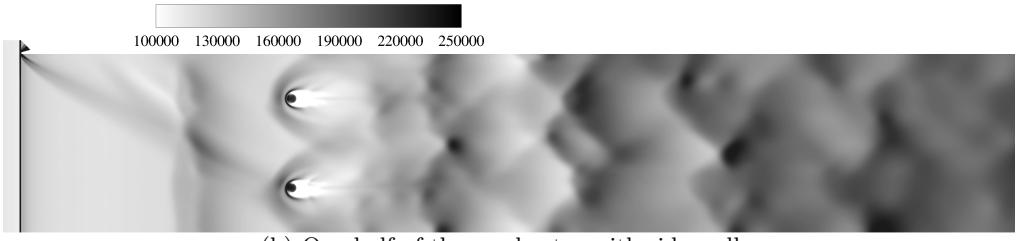

(b) One half of the combustor with side walls.

FIGURE 3. Contour of pressure in a plane parallel to the bottom wall of the combustor located at $y/d = 0.25$.

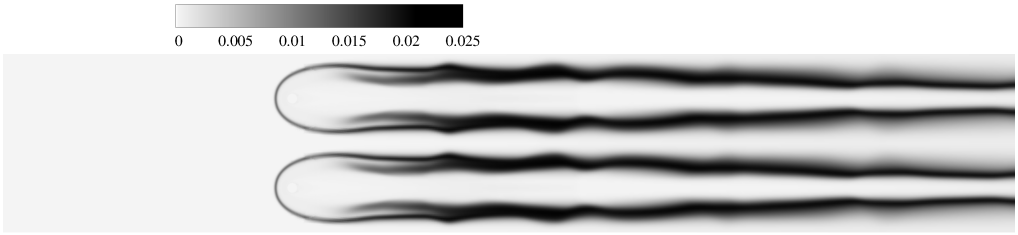

(a) One eighth of the combustor without side walls (mirrored four times).

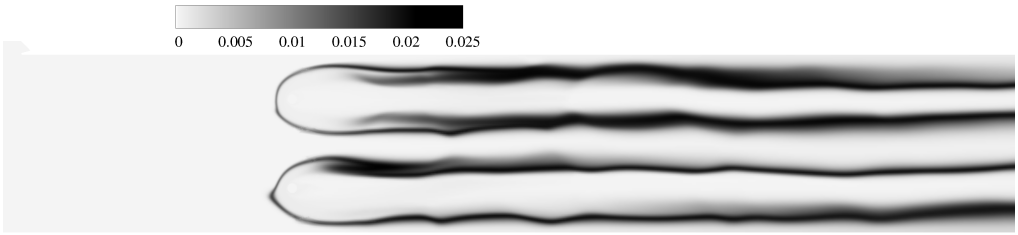

(b) One half of the combustor with side walls.

FIGURE 4. Contour of OH mass fraction in a plane parallel to the bottom wall of the combustor located at $y/d = 0.25$.

The location of this normal shock moves upstream with increasing fuel flow rate. Note that the shock train is still present behind the normal shock, demonstrating the flow behind the normal shock is not completely subsonic. This is confirmed in Figure 6, where the ratio of subsonic cross-area to the total cross-area is shown. Approximately half of the combustor area is subsonic between the first normal shock and the beginning of the exhaust nozzle.

The large pressure increase is caused by the additional heat release due to higher fuel flow rate. This is illustrated in Figures. 7 and 8 where contours of temperature and water

Equivalence ratio [-]	0.30	0.35	0.40	0.45	0.50
Total pressure [bar]	5.00	5.83	6.65	7.48	8.30

TABLE 1. Total pressure and temperature used in the injector plenum for different equivalence ratios.

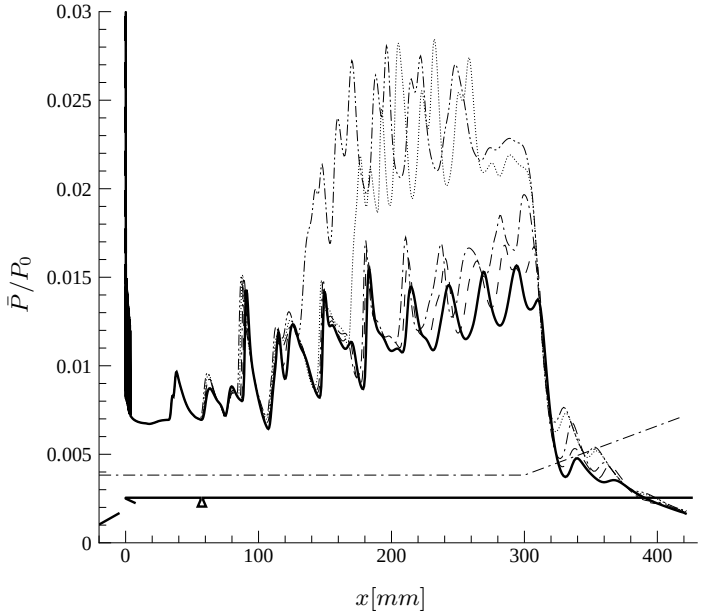

FIGURE 5. Pressure along the bottom wall of the combustor between two hydrogen injectors (one eighth of the combustor without side walls). Nominal condition $\phi = 0.3$, thick continuous line; $\phi = 0.35$, dashed line; $\phi = 0.4$, dash-dot line; $\phi = 0.45$, dotted line; and $\phi = 0.5$, dash-dot-dot line.

mass fraction (i.e., progress variable) are shown in a plane passing through the injector. The overall temperature in the combustor is much higher for $\phi = 0.5$ (Figure 7(b)). The entire height behind the injector becomes subsonic, as indicated by the sonic line. As expected, the position of the normal shock correlates directly with the strong temperature increase. Figure 8 also indicates that ignition takes place more upstream at $\phi = 0.5$. The shear layer between the jet and the cross-flow also shows burning regions in the case of high fuel flow rate. While combustion takes place in the lower half of the combustor for $\phi = 0.3$, the higher jet momentum ratio for $\phi = 0.5$ causes the flame to reach the upper wall (cowl side).

A clear and abrupt change in the flow characteristics occurs between $\phi = 0.4$ and $\phi = 0.45$, that can be identified as the inception of unstart. Yet, the combustor is not completely choked and a part of the flow, i.e., between two injectors, is still supersonic. However, the large increase in pressure (almost twice the maximum pressure compared to the nominal case) could already reach the design margins and impose undesired stress on the structure.

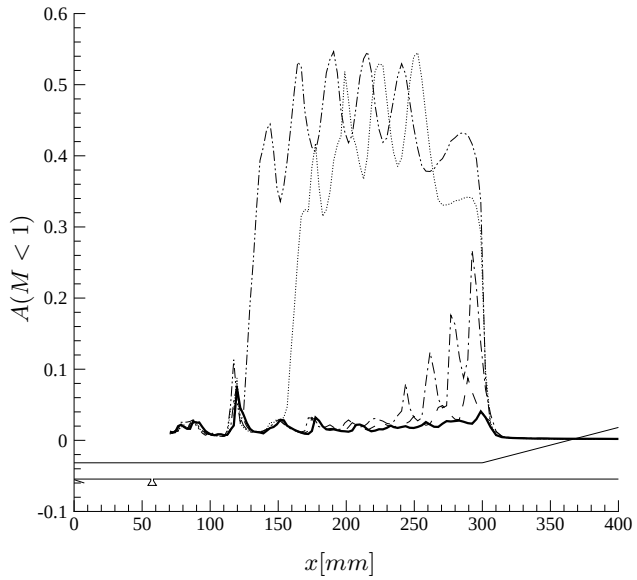

FIGURE 6. Ratio of subsonic cross-area to total cross-area. Nominal condition $\phi = 0.3$, thick continuous line; $\phi = 0.35$, dashed line; $\phi = 0.4$, dash-dot line; $\phi = 0.45$, dotted line; and $\phi = 0.5$, dash-dot-dot line.

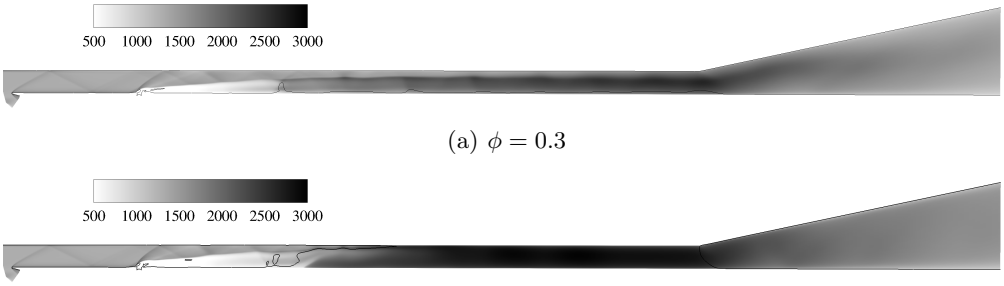

(a) $\phi = 0.3$

(b) $\phi = 0.5$

FIGURE 7. Contour of temperature in a symmetry plane across one injector (one eighth of the combustor without side walls) and sonic line (continuous line)

4. Conclusions and future work

The present study describes a combustion model for high-speed flows. The model is tested in the HyShot II case and simulation results compare well with experimental measurements. The model is then used to investigate the inception of the unstart phenomenon due to thermal choking by increasing the fuel flow rate. It is shown that an abrupt change occurs between $\phi = 0.4$ and $\phi = 0.45$, where a normal shock forms and moves upstream accompanied by a large region of subsonic flow. Nevertheless, the combustor is not completely choked and part of the flow is still supersonic.

The next steps will focus on improving the combustion model. In particular, compressibility effects on the chemistry will be considered. Additionally, the inception of unstart will be better characterized and additional equivalence ratios between $\phi = 0.4$ and $\phi = 0.45$ will be investigated. Finally, the dependence of this inception point on turbulence, geometry and combustion models and other uncertainties will be studied.

(a) $\phi = 0.3$

(b) $\phi = 0.5$

FIGURE 8. Contour of water mass fraction (progress variable) in a symmetry plane across one injector (one eighth of the combustor without side walls) and sonic line (continuous line).

Acknowledgments

The authors would like to thank Dr. K. Hannemann and S. Karl (German Aerospace Center, DLR, Germany) for providing the experimental data. This material is based upon work supported by the Department of Energy [National Nuclear Security Administration] under the Predictive Science Academic Alliance Program (PSAAP) at Stanford University, Award Number(s) DE-FC52-08NA28614.

REFERENCES

BATES, R. W., GOLDEN, D. M., HANSON, R. K. & BOWMAN, C. T. 2001 Experimental study and modeling of the reaction $H+O_2+M \rightarrow HO_2 + M$ (M=Ar, N_2, H_2O) at elevated pressures and temperatures between 1050 and 1250 K. *Phys. Chem. Chem. Phys.* **3**(12), 2337–2342.

BAURLE, R., HSU, A. & HASSAN, H. 1995 Assumed and evolution probability density functions in supersonic turbulent combustion calculations. *J. Propul. Power* **11**(6), 1132–1138.

BAURLE, R. & GIRIMAJI, S. 2003 Assumed PDF turbulence-chemistry closure with temperature-composition correlations. *Combust. Flame* **134**, 131–148.

BERGLUND, M. & FUREBY, C. 2007 LES of supersonic combustion in a scramjet engine model. *Proc. Combust. Inst.* **31**, 2497–2504.

BIRZER, C. & DOOLAN, C.J. 2007 Quasi-one-dimensional modeling of hydrogen fueled scramjet combustors. *AIAA 2007-4314*.

BIRD, R.B., STEWART, W.E. & LIGHTFOOT, E.N. 2007 *Transport Phenomena*, John Wiley & Sons, Inc.

BOYCE, R.R., GERARD, S. & PAULL, A. 2003 The HyShot scramjet flight experiment - flight data and CFD calculations compared. *AIAA 2003-7029*.

CHAKRABORTY, D., PAUL, P. & MUKUNDA, H. 2000 Evaluation of combustion models for high speed H2/air confined mixing layer using DNS data. *Combust. Flame* **121**, 195–209.

COOK, D. J., PITSCH, H., CHEN, J. H. & HAWKES, E. R. 2007 Flamelet-based modeling of auto-ignition with thermal inhomogeneities for application to HCCI engines. *Proc. Combust. Inst.* **31**, 2903–2911.

FUREBY, C., CHAPUIS, M., FEDINA, E. & KARL, S. 2010 CFD analysis of the HyShot II scramjet combustor. *Proc. Comb. Inst.* (in press).

Gardner, A. D., Hannemann, K., Steelant, J. & Paull, A. 2004 Ground testing of the HyShot supersonic combustion flight experiment in HEG and comparison with flight data. *AIAA 2004-3345*.

Genin, F., Chernyavsky, B. & Menon, S. 2004 Large eddy simulation of scramjet combustion using a subgrid mixing/combustion model. *AIAA 2004-7035*.

Hannemann, K., Karl, S., Martinez Schramm, J. & Steelant, J. 2010 Methodology of a combined ground based testing and numerical modeling analysis of supersonic combustion flow paths. *Shock Waves* **20**(5), 353–366.

Hass, N.E., Smart, M.K. & Paull, A. 2005 Flight data analysis of HyShot 2. *AIAA 2005-3354*.

Herbon, J. T., Hanson, R. K., Golden, D. M. & Bowman C. T. 2002 A shock tube study of the enthalpy of formation of OH. *Proc. Combust. Inst.* **29**, 1201–1208.

Ihme, M., Cha, C. M. & Pitsch, H. 2005 Prediction of local extinction and re-ignition effects in non-premixed turbulent combustion using a flamelet/progress variable approach. *Proc. Combust. Inst.* **30**, 793–800.

Ingenito, A., Bruno, C. & Cecere, D. 2010 LES of the HyShot scramjet combustor. *AIAA 2010-758*.

Karl, S., Hannemann, K., Mack, A. & Steelant, J. 2008 CFD analysis of the HyShot II scramjet experiments in the HEG shock tunnel. *AIAA 2008-2548*.

Karl, S., Hannemann, K., Steelant, J. & Mack, A. 2006 CFD analysis of the HyShot supersonic combustion flight experiment configuration. *AIAA 2006-8041*.

Kindler, M., Lempke, M., Blacha, T., Gerlinger, P. & Aigner, M. 2008 Numerical investigation of the HyShot supersonic combustion configuration. *AIAA 2005-3355*.

Kodera, M., Sunami, T. & Itoh, K. 2005 Numerical simulation of a scramjet engine for JAXA's flight experiment using HyShot. *AIAA 2005-3355*.

Pecnik, R., Constantine, P., Ham, F. & Iaccarino, G. 2008 A probabilistic framework for high-speed flow simulations. *Annual Research Briefs 2008*. Center for Turbulence Research, Stanford University/NASA Ames, 3–17.

Pecnik, R., Terrapon, V.E., Ham, F. & Iaccarino, G. 2009 Full system scramjet simulation. *Annual Research Briefs 2009*. Center for Turbulence Research, Stanford University/NASA Ames, 33–45.

Peters, N. 2000 *Turbulent Combustion*, Cambridge University Press.

Pierce, C. D. & Moin, P. 2004 Progress-variable approach for large-eddy simulation of non-premixed turbulent combustion. *J. Fluid Mech.* **504**, 73–97.

Pitsch, H. 2006 Large-eddy simulation of turbulent combustion. *Annu. Rev. Fluid Mech.* **38**, 453–382.

Schramm, J.M., Karl, S., Hannemann, K. & Steelant, J. 2008 Ground testing of the HyShot II scramjet configuration in HEG. *AIAA 2008-2547*.

Smart, M. K., Hass, N. E. & Paull, A. 2006 Flight data analysis of the HyShot 2 scramjet flight experiment. *AIAA Journal* **44**(10), 2366–2375.

Steelant, J., Mack, A., Hannemann, K. & Gardner, A.D. 2006 Comparison of supersonic combustion tests with shock-tunnels, flight and CFD. *AIAA 2006-4684*.

Terrapon, V.E., Pecnik, R., Ham, F. & Pitsch, H. 2009 A flamelet-based model for supersonic combustion. *Annual Research Briefs 2009*. Center for Turbulence Research, Stanford University/NASA Ames, 47–58.